# Analysis of scanning thermal microscopy measurements on CVD graphene

*Original*
Analysis of scanning thermal microscopy measurements on CVD graphene / Zhang, Han; Napolitano, Andrea; Tortello, Mauro. - In: APPLIED PHYSICS LETTERS. - ISSN 0003-6951. - ELETTRONICO. - 128:17(2026), pp. 1-7. [10.1063/5.0320106]

*Publisher:*
American Institute of Physics - AIP

*Published*
DOI:10.1063/5.0320106

Applied Physics Letters

RESEARCH ARTICLE | APRIL 27 2026

# Analysis of scanning thermal microscopy measurements on CVD graphene

**Special Collection:** Thermal Properties of Graphene and Carbon Materials – From Physics to Applications in Thermal Management

Han Zhang ; Andrea Napolitano ; Mauro Tortello

*Appl. Phys. Lett.* 128, 172201 (2026)
https://doi.org/10.1063/5.0320106

AIP Publishing

Applied Physics Letters ARTICLE pubs.aip.org/aip/apl

# Analysis of scanning thermal microscopy measurements on CVD graphene

Cite as: Appl. Phys. Lett. **128**, 172201 (2026); doi: 10.1063/5.0320106
Submitted: 29 December 2025 · Accepted: 6 April 2026 ·
Published Online: 27 April 2026

Han Zhang, Andrea Napolitano, and Mauro Tortello[a)]

AFFILIATIONS

Dipartimento Scienza Applicata e Tecnologia, Politecnico di Torino, Cso Duca degli Abruzzi 24, 10129 Torino (TO), Italy

**Note:** This paper is part of the Special Topic, Thermal Properties of Graphene and Carbon Materials—From Physics to Applications in Thermal Management.

[a)]Author to whom correspondence should be addressed: mauro.tortello@polito.it

## ABSTRACT

Scanning thermal microscopy (SThM) results on chemical vapor-deposited graphene supported by different substrates have been analyzed by the finite-element method (FEM). The analysis has been validated by using the results of a simplified lumped-element model in which graphene is schematized as an isotropic material in perfect contact with the substrate, as reported in Tortello *et al.*, ACS Appl. Nano Mater. **2**, 2621–2633 (2019). Subsequently, the model has been employed to obtain a semi-quantitative estimation of the graphene in-plane thermal conductivity, which was found in agreement with other reports. The combined use of SThM and FEM, possibly complemented with supplementary results, e.g., from thermoreflectance experiments, offers interesting possibilities to study graphene and 2D materials with the unique spatial resolution of SThM, especially in view of nanoscale heat transfer and heat management applications.

The discovery of graphene[1] and its exceptional electronic, mechanical, and thermal properties[2–4] marked the beginning of an intense research on 2D and related materials.[5–7] In particular, the study of the nanoscale thermal properties of 2D materials[8–11] is very important because the continuous miniaturization of the electronic circuits, the increase in their usage in AI, and high performance computing applications,[12,13] with the subsequent increase in heat dissipation per surface unit, require efficient heat management strategies.[14–16] Moreover, these studies can also be relevant from a more fundamental point of view, because several non-Fourier heat conduction mechanisms can occur at the nanoscale, such as the quasi-ballistic, hydrodynamic, and coherent regimes.[17–19] Given their reduced thickness and anisotropic properties, e.g., the high in-plane thermal conductivity of graphene, these materials can be used as efficient protective coatings[20–22] or heat spreaders.[23–25] When dealing with heat management at the nanoscale, the interface between the 2D material and its support has also to be taken into account. Therefore, the thermal boundary resistance (TBR)[26] for different types of graphene, e.g., exfoliated, grown by chemical vapor deposition (CVD), encased, etc., has been extensively studied.[27–31] Scanning thermal microscopy (SThM) is a powerful technique to study the heat transfer properties at the nanoscale.[32–36] While it may not be immediate to obtain quantitative information,[37–40] the lateral spatial resolution of SThM is almost unmatched, as it can be as low as tens of nanometers.[41] Other methods, for example, the Raman optothermal technique,[11] are limited by the wavelength of the incident radiation. In Ref. 42, we performed SThM experiments and characterized the heat transfer properties of one layer of CVD graphene supported by different substrates whose thermal conductivity spans three orders of magnitude. In the case of the $SiO_2$ substrate, the effect of two and four layers was studied as well. By using a lumped-element model and by considering graphene as an isotropic material in perfect contact with the substrate, we showed that the thermal conductivity in the monolayer case, for perpendicular heat injection, is equivalent to that of a material with thermal conductivity equal to $k_{eff} = 2.5 \pm 0.3\,\mathrm{W/m\,K}$ and thickness $t = 3.5 \pm 0.3\,\mathrm{nm}$. The value found for the thermal conductivity, apparently, might seem very small, given the high conductivity of graphene. However, it was obtained in the case of heat injection perpendicular to the plane and also included the TBR between graphene and the substrate. Here, with the help of finite-element analysis (FEA), we report on a more comprehensive and thorough study of those experiments and provide an estimation of the in-plane conductivity of graphene, which is found to be about

$k_{ab} = 300 \pm 200\,\mathrm{W/(m\,K)}$, in good agreement with values reported in the literature by other techniques. The combination of SThM and finite-element analysis, reported here, can be applied for the investigation of the thermal properties of 2D and layered materials.

The most popular type of SThM probe is probably the one based on the change in the electrical resistance of a metal or a doped semiconductor.[34] SThM resistive probes are part of a Wheatstone bridge, as shown in Fig. 1(a). Since the resistance of a metal or a semiconductor is dependent on the temperature, a change in temperature produces a change in the bridge voltage. By knowing the temperature coefficient of the probe, the temperature variation can be measured while scanning, thanks to its direct relation with the electrical properties. In general, the temperature variation of the probe is related to the thermal conductivity of the sample: when the tip is on a more thermally conducting region, the heat flux will be larger, and thus the temperature will decrease, compared to a less conducting area. In this work, we will consider nanofabricated probes, in which the active element is a thin Pd film that can act at the same time as a heater, via the Joule effect, and as a thermometer. These are often called the Pd probes and usually have a curvature radius that is smaller than 100 nm, allowing us to obtain a thermal resolution of the order of a few tens of nanometers.[42] Pd is deposited on $Si_3N_4$ and is connected to the cantilever by means of an Au film,[43] as reported in Figs. 1(b) and 1(c), which shows scanning electron microscope (SEM) measurements of one of our probes that have been used to create a geometrical model for the finite-element analysis, in good accordance with other reports.[44] Panel (d) reports an example of measured thicknesses of different materials. In particular, the thickness of the Pd film is found to be around 43 nm, considering a 5 nm thick NiCr layer, which is in agreement with the expected nominal thickness of 40 nm.

In order to investigate the heat transfer mechanism between the probe and graphene supported by different substrates, a thermal-electrical simulation model is developed by using the commercial software COMSOL Multiphysics 6.3. More detailed information on the model adopted for the SThM probe is reported in the supplementary material. The investigated samples consist of one or more chemical vapor-deposited graphene layers on a substrate, as shown in Fig. 2(a). The substrate can be polyethylene terephthalate (PET), $SiO_2$, or $Al_2O_3$ (alumina), so that their thermal conductivity spans three orders of magnitude, corresponding to 0.2, 1.4, and 15 W/m K, respectively. In Ref. 42, we adopted a lumped-element model and considered graphene as an isotropic material in *perfect* contact with the substrate, as sketched in Fig. 2(b). This assumption simplified the analysis by avoiding the determination of the TBR between graphene and the substrates and the inclusion in the model of the highly anisotropic thermal conductivity of graphene. In this way, the effective thermal conductivity seen by the SThM probe could be determined as well as the equivalent effective thickness of the isotropic material. One graphene layer was found to have an effective thickness $t_{eff} = 3.5 \pm 0.3\,\mathrm{nm}$, while for two

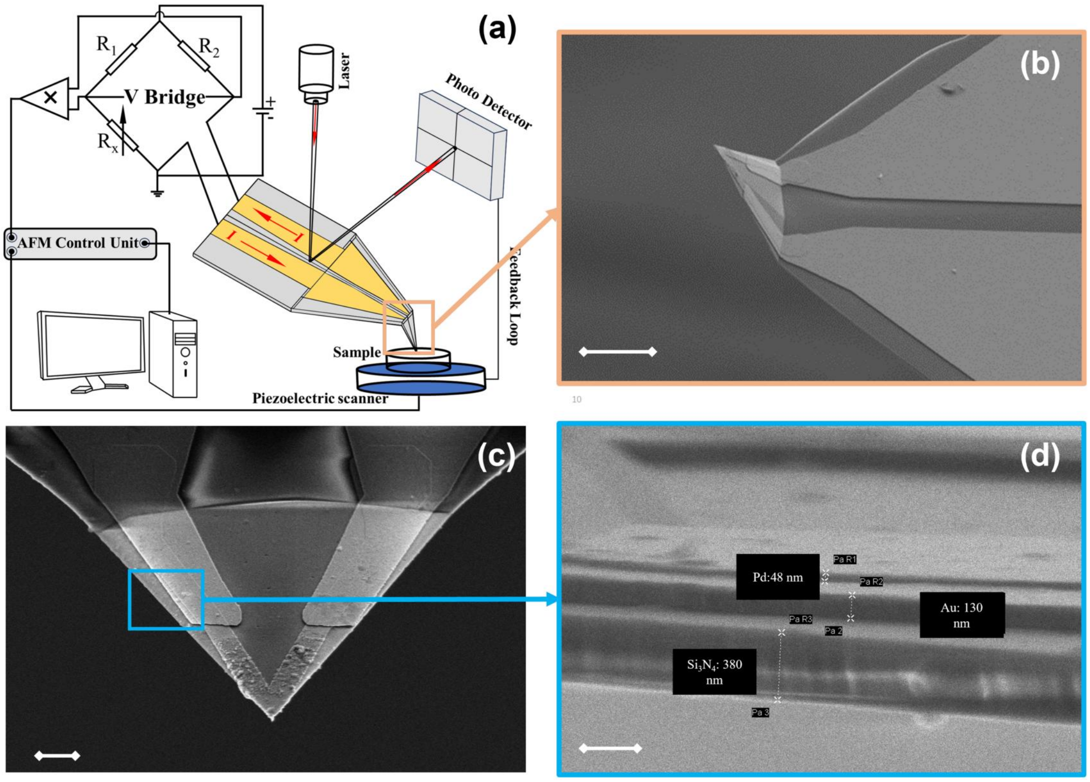

**FIG. 1.** SThM working principle and Pd probe structure. (a) The SThM resistive probe is part of a Wheatstone bridge. (b) SEM image of a Pd probe, namely VITA-HE-GLA by Bruker. (c) Magnification of (b). (d) Magnification of (c), where the thickness of the different materials, $Si_3N_4$, Au, and Ni/Cr + Pd, can be observed. Scale bars in (b), (c), and (d) are 10 $\mu$m, 2 $\mu$m, and 300 nm long, respectively.

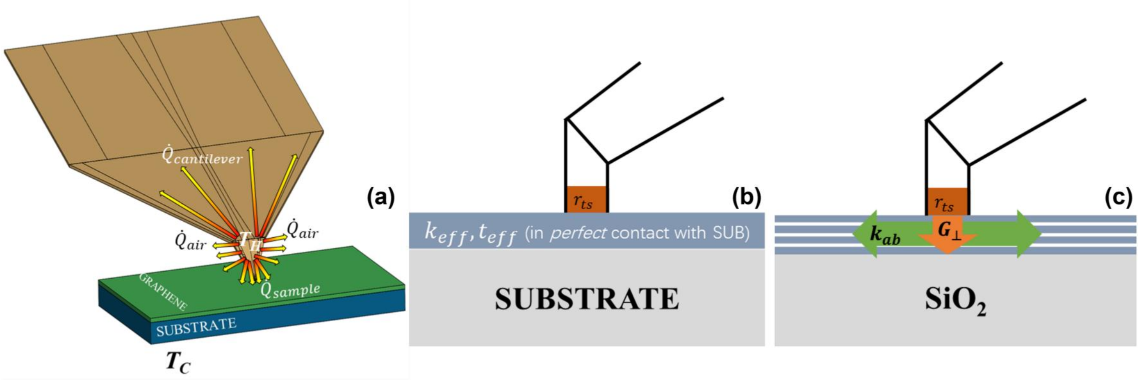

**FIG. 2.** (a) Sketch of the SThM probe in contact with CVD graphene supported by a substrate. The different heat conduction channels are visible, from the heater ($T_H$) to ambient temperature ($T_C$), through the cantilever, air, and sample. (b) Isotropic model for graphene in perfect contact with the substrate. $r_{ts}$, represented by a thick element at the tip apex, is the tip-sample thermal boundary resistance. (c) Anisotropic model for graphene. $G_\perp$ is the perpendicular thermal conductance and $k_{ab}$ is the in-plane thermal conductivity of graphene.

and four graphene layers on the SiO$_2$ substrate, we have $t_{2-eff} = 7.6 \pm 3.5$ nm and $t_{4-eff} = 26 \pm 12$ nm, respectively. The larger effective thickness in the four-layer case was attributed to the decreasing detrimental effect of the substrate on thermal properties as the number of layers increases; this effect was not yet visible in the two-layer case. In the first part of our study, we will use this model for the sample (represented in COMSOL by a layered shell) to validate our finite-element analysis. Subsequently, we will consider the anisotropic properties of graphene and estimate its in-plane thermal conductivity, $k_{ab}$.

As it was done in the experiments, to reduce the experimental uncertainty,[42] we will consider the difference between the temperature of the probe on the bare substrate and the temperature of the probe on the supported graphene. Indeed, scanning the tip across graphene and then on the sample in the same measurements ensured more reliable data that can be compared with simulations. The temperature variations are of the order of tens or hundreds of millikelvin at most.

Panels (a)–(d) in Fig. 3 report the temperature map of the SThM probe in contact with different samples, as obtained by the simulations. The thermal conductivity is progressively increasing from air,

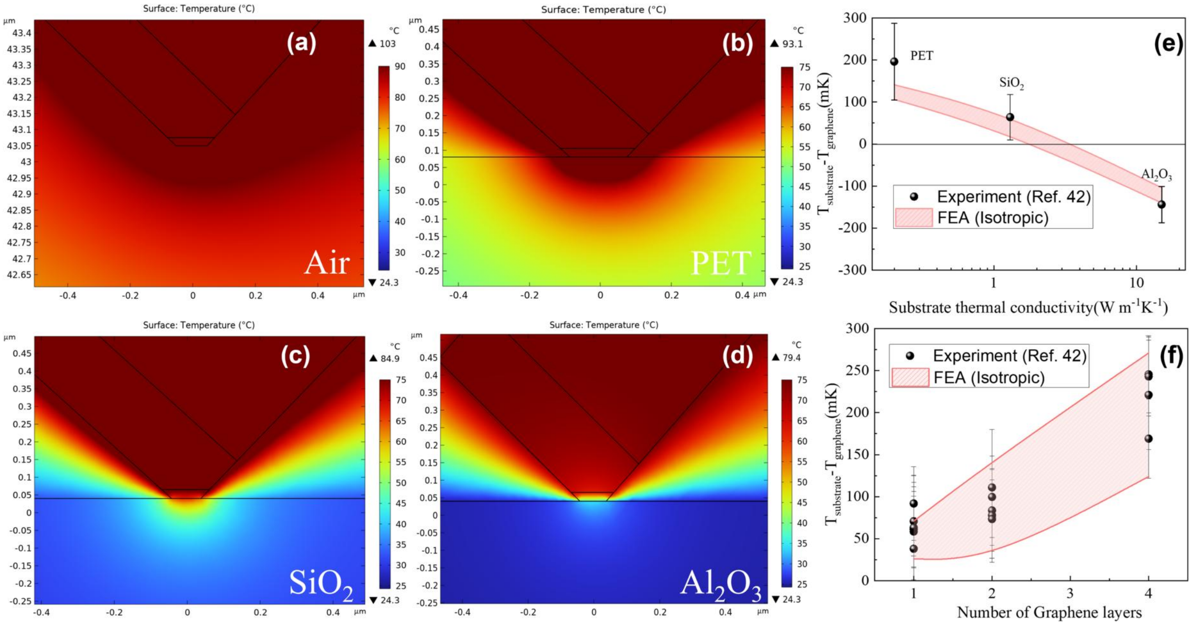

**FIG. 3.** (a)–(d) SThM probe in air and in contact with different substrates: Air, PET, SiO$_2$, and Al$_2$O$_3$, respectively. The contact radii are $r = 90$ nm in (b) and $r = 58$ nm in (c) and (d). (e) Symbols: experimental[42] $\Delta T = T_{substrate} - T_{graphene}$ for graphene supported by different substrates. Red band: FEA simulation results with $k_{eff} = 2.5 \pm 0.3$ W/(m K) and $t_{eff} = 3.5 \pm 0.3$ nm. (f) Same as in (e) but for one, two, and four CVD graphene layers supported by SiO$_2$.

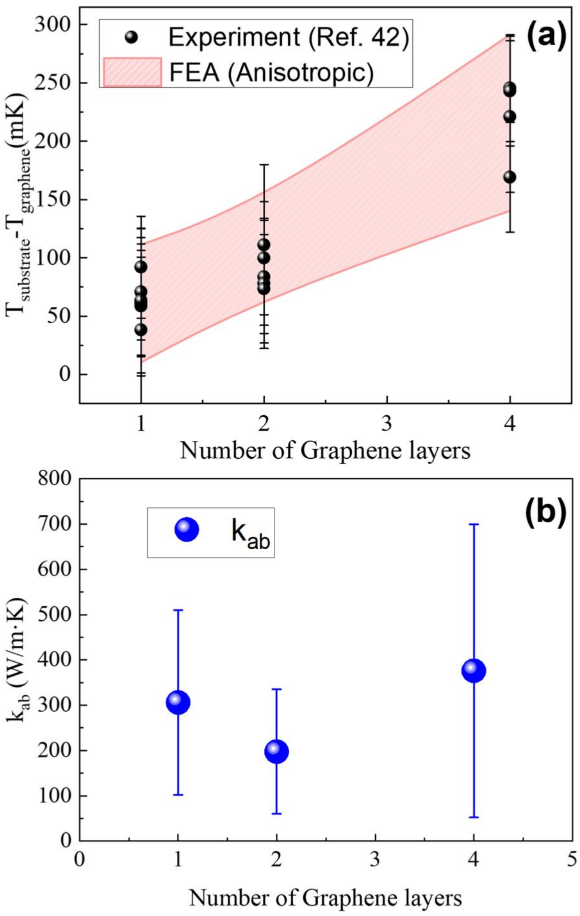

**FIG. 4.** (a) Symbols: experimental[42] $\Delta T = T_{substrate} - T_{graphene}$ for one, two, and four CVD graphene layers supported by $SiO_2$. Red band: FEA simulation results accounting for the anisotropic thermal conductivity of graphene. (b) Graphene in-plane thermal conductivity, $k_{ab}$ used in the FEA simulations reported in (a). Error bars come from the uncertainty on $G_\perp$ used to determine $k_c$.

in panel (a), to $Al_2O_3$, panel (d). As expected, it is possible to notice that, in the region of the contact, when moving away from the heat source, the temperature is decreasing faster with increasing thermal conductivity of the substrate. As a consequence, also the depth at which the room temperature is recovered in the bulk decreases accordingly. These situations correspond to a different average temperature of the probe, namely $T_{probe} = 76.8$, 69.0, 63.0, and 60.2 °C, for air, PET, $SiO_2$, and $Al_2O_3$, respectively. Symbols in panel (e), with the relevant error bars, represent the experimental tip temperature variation, $\Delta T = T_{substrate} - T_{graphene}$, as obtained in the case of a single graphene layer supported by different substrates.[42] The red band represents the $\Delta T$ range as can be obtained by FEA. All the simulations have been performed by varying the following quantities within the range determined in Ref. 42, i.e., $r_{ts} = 2.4 \pm 0.6\ \mathrm{Km^2/W}$ and $r = 20$–60 nm for the contact radius in the case of $SiO_2$ and $Al_2O_3$ and $r = 60$–90 nm for PET. The electrical current was the same as that used in the experiments, i.e., 1.35 mA, while the thickness of the Pd film was set to 37.5 nm. Actually, this quantity was the only free parameter, slightly tuned around the nominal value of 40 nm, to obtain a reasonable match with the data and subsequently always kept constant. In panel (e), it is possible to notice that the FEA is able to reproduce part of the experimental data, although not the highest $\Delta T$s for graphene supported by PET and $SiO_2$ and the lowest ones for $Al_2O_3$. However, there are no other free parameters in the FEA, and it is worth pointing out that not all experiments have been performed with the same probe. Therefore, the additional scattering might be caused by the obvious slight physical variations that occur from probe to probe. Panel (f) reports the same analysis for the case of one, two, and four CVD layers supported by $SiO_2$. The only difference with respect to the previous case is the effective thickness for the two and four layers. The capability of the finite-element model to reproduce the experimental data is very good, and it is now possible to reproduce most of the experimental data for 2 and 4 layers. This is due to their larger relative uncertainty on the effective thickness, which is 12% for one layer and 46% for the two and four layers, as already shown before.

The results reported above demonstrate that the finite-element analysis is capable of reproducing all the experimental temperature variations by using the same parameters obtained in the lumped-element analysis reported in Ref. 42. Therefore, it is now possible to investigate in more detail the thermal conduction properties of the samples, which had been partly hidden in the use of effective thermal conductivity and effective thickness. The perpendicular thermal conduction of the supported mono- and multi-layer graphene has been extensively measured, also in the case of multiple-stacked CVD graphene,[27] as it is the case discussed here. Therefore, we can use the experimental range for the perpendicular thermal conductance, $G_\perp$, as reported in Ref. 27, and the experimental thickness of one, two, and four graphene layers on $SiO_2$, $t_n$, $n = 1, 2, 4$, to solve the one-parameter inverse problem and estimate the possible range of the in-plane thermal conductivity, $k_{ab}$. The range of the perpendicular thermal conductivity, $k_c$ can be estimated from $G_\perp$ and $t_n$ by using the Kapitza length, $\lambda = R_\perp k_c$, where we considered $\lambda = t_n - nt_{GR}$ and $t_{GR} = 0.34$ nm. $t_n$ has been determined from the AFM measurements as $t_1 = 0.98 \pm 0.17$ nm, $t_2 = 2.16 \pm 0.47$ nm, and $t_4 = 3.97 \pm 0.96$ nm. These values are in agreement with those reported in other works,[45] considering the presence of adsorbate layers between the substrate and the stacked layers.[42] The anisotropic thermal conductivity was represented in COMSOL by a second-rank diagonal tensor containing $k_{ab}$ and $k_c$. Figure 4(a) shows the comparison between the experimental temperature variation, $\Delta T$ as a function of the number of layers (symbols), and the simulated results (red band) obtained by keeping the same range of parameters used in the isotropic study and sweeping $k_{ab}$ within the $k_c$ range determined above. Figure 4(b) reports the obtained values of $k_{ab}$ in the three cases analyzed. First of all, it is possible to note that the range of obtained values is well within the range reported for supported graphene.[27,28,46] The error bars are quite large due to the relatively large scattering of experimental data for $G_\perp$. It is not possible to deduce a clear trend of $k_{ab}$ as a function of the number of layers due to the large uncertainty, even if there might be a slight decrease in the two layer case, followed by an increase in $k_{ab}$ for four layers. A possible explanation of this trend could be that, as shown in Ref. 42, the two layer sample features a larger amount of defects, inclusions, and wrinkles on the surface compared to the other samples. Therefore, the addition of a second graphene layer was not particularly effective in improving thermal conduction. On the

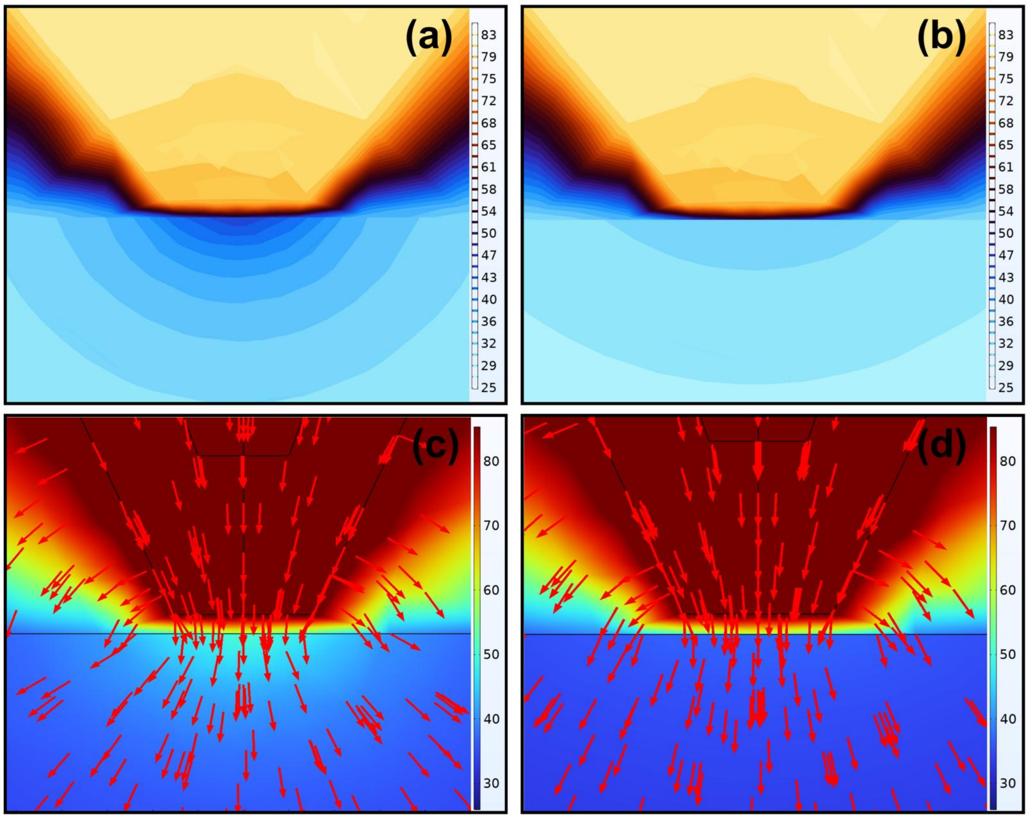

**FIG. 5.** (a) Temperature contours for the probe in contact with four graphene layers on $SiO_2$ substrate, in the isotropic model case. (b) Same as in (a) but for the anisotropic case, $k_{ab} = 110\,\mathrm{W/m\,K}$. (c) Heat flux lines for the isotropic case. (d) Same as in (c) but for the anisotropic case.

contrary, when four layers are subsequently stacked one on top of the other, the heat conduction properties improve and the detrimental effect of the substrate becomes less relevant.[11,24]

Figure 5 reports the temperature contours and heat flux lines for the effective isotropic (left) and anisotropic (right) models for graphene, respectively. Panel (a) clearly shows that the temperature is radially decreasing from the hot contact region between probe and sample toward the bulk of the substrate. In panel (b), on the contrary, it can be seen that the temperature decrease is no longer radial but more distributed in the horizontal direction, indicating the higher in-plane conductivity of graphene that makes it interesting for heat spreading applications. Since the heat is dissipated faster in the horizontal direction, the depth of the heated material is also lower compared to the isotropic case. Panels (c) and (d) compare, for the two cases, the heat flux lines from the hot probe to the bulk of the sample. The heat flow from the probe to the sample through the air looks very similar in the two situations. This is not the case for the heat flux into the sample. While the lines depart more or less radially from the contact region into the sample for the isotropic model, they are more perpendicular to the graphene/substrate interface in the anisotropic case. This is again due to the fact that, since the heat now spreads faster in the graphene plane, it subsequently flows more uniformly from graphene into the bulk, giving rise to more perpendicular lines. We can notice that the effective isotropic model, used also in Ref. 42, is very useful for representing what is seen by the SThM probe in terms of heat transfer, but lacks the capability to give more information on the heat conduction properties of the sample, when the latter is not simply a bulk material, but is, for example, multilayered and/or anisotropic. On the contrary, the anisotropic model, with the inclusion of the perpendicular thermal conductance determined by independent experiments, allows us to obtain a good, semi-quantitative estimation of the in-plane thermal conductivity of the samples.

The results reported here show that the combined use of SThM and finite-element analysis can be effectively used to characterize the thermal properties of 2D materials beyond a mere qualitative investigation. First, the model needs to be validated. Here, this has been achieved by comparing it with the outcome obtained by a lumped-element analysis, but it could also be done by comparing the model with experimental results from calibration samples with known thermal conductivity. Then, the thermal properties of the material under study can be determined. In particular, in the case of anisotropic and layered materials, some complementary information from independent experiments is desirable in order to suitably invert the problem and estimate some specific physical quantities, such as, in this case, the graphene in-plane thermal conductivity. In this way, the unmatched lateral spatial resolution of SThM can be exploited more efficiently for the characterization of this class of materials, particularly relevant and promising for nanoscale heat transfer and heat management applications.

See the supplementary material for additional information regarding the finite-element model of the SThM probe, and discussion on the possible non-diffusive heat transfer mechanisms, temperature-induced deformations, and the effect of natural convection.

## AUTHOR DECLARATIONS

### Conflict of Interest

The authors have no conflicts to disclose.

### Author Contributions

**Han Zhang**: Data curation (lead); Formal analysis (lead); Investigation (lead); Methodology (equal); Software (supporting); Validation (equal); Visualization (equal); Writing – original draft (supporting); Writing – review & editing (equal). **Andrea Napolitano:** Data curation (supporting); Formal analysis (supporting); Investigation (supporting); Methodology (equal); Software (lead); Validation (equal); Writing – review & editing (equal). **Mauro Tortello:** Conceptualization (lead); Data curation (supporting); Formal analysis (supporting); Investigation (supporting); Methodology (equal); Project administration (lead); Resources (lead); Software (supporting); Supervision (lead); Validation (equal); Visualization (equal); Writing – original draft (lead); Writing – review & editing (equal).

## DATA AVAILABILITY

The data that support the findings of this study are available from the corresponding author upon reasonable request.

## REFERENCES

[1] K. S. Novoselov, A. K. Geim, S. V. Morozov, D. Jiang, Y. Zhang, S. V. Dubonos, I. V. Grigorieva, and A. A. Firsov, "Electric field effect in atomically thin carbon films," Science **306**, 666–669 (2004).

[2] A. H. Castro Neto, F. Guinea, N. M. R. Peres, K. S. Novoselov, and A. K. Geim, "The electronic properties of graphene," Rev. Mod. Phys. **81**, 109–162 (2009).

[3] G. Wang, H. Hou, Y. Yan, R. Jagatramka, A. Shirsalimian, Y. Wang, B. Li, M. Daly, and C. Cao, "Recent advances in the mechanics of 2D materials," Int. J. Extreme Manuf. **5**, 032002 (2023).

[4] A. A. Balandin, S. Ghosh, W. Bao, I. Calizo, D. Teweldebrhan, F. Miao, and C. N. Lau, "Superior thermal conductivity of single-layer graphene," Nano Lett. **8**, 902 (2008).

[5] C. Backes, A. M. Abdelkader, C. Alonso, A. Andrieux-Ledier, R. Arenal, J. Azpeitia, N. Balakrishnan, L. Banszerus, J. Barjon, R. Bartali, S. Bellani, C. Berger, R. Berger, M. M. Ortega, C. Bernard, P. H. Beton, A. Beyer, A. Bianco, P. Bøggild, F. Bonaccorso, G. B. Barin, C. Botas, R. A. Bueno, D. Carriazo, A. Castellanos-Gomez, M. Christian, A. Ciesielski, T. Ciuk, M. T. Cole, J. Coleman, C. Coletti, L. Crema, H. Cun, D. Dasler, D. D. Fazio, N. Díez, S. Drieschner, G. S. Duesberg, R. Fasel, X. Feng, A. Fina, S. Forti, C. Galiotis, G. Garberoglio, J. M. García, J. A. Garrido, M. Gibertini, A. Gölzhäuser, J. Gómez, T. Greber, F. Hauke, A. Hemmi, I. Hernandez-Rodriguez, A. Hirsch, S. A. Hodge, Y. Huttel, P. U. Jepsen, I. Jimenez, U. Kaiser, T. Kaplas, H. K. Kim, A. Kis, K. Papagelis, K. Kostarelos, A. Krajewska, K. Lee, C. Li, H. Lipsanen, A. Liscio, M. R. Lohe, A. Loiseau, L. Lombardi, M. F. López, O. Martin, C. Martín, L. Martínez, J. A. Martin-Gago, J. I. Martínez, N. Marzari, Á. Mayoral, J. McManus, M. Melucci, J. Méndez, C. Merino, P. Merino, A. P. Meyer, E. Miniussi, V. Miseikis, N. Mishra, V. Morandi, C. Munuera, R. Muñoz, H. Nolan, L. Ortolani, A. K. Ott, I. Palacio, V. Palermo, J. Parthenios, I. Pasternak, A. Patane, M. Prato, H. Prevost, V. Prudkovskiy, N. Pugno, T. Rojo, A. Rossi, P. Ruffieux, P. Samorì, L. Schué, E. Setijadi, T. Seyller, G. Speranza, C. Stampfer, I. Stenger, W. Strupinski, Y. Svirko, S. Taioli, K. B. Teo, M. Testi, F. Tomarchio, M. Tortello, E. Treossi, A. Turchanin, E. Vazquez, E. Villaro, P. R. Whelan, Z. Xia, R. Yakimova, S. Yang, G. R. Yazdi, C. Yim, D. Yoon, X. Zhang, X. Zhuang, L. Colombo, A. C. Ferrari, and M. Garcia-Hernandez, "Production and processing of graphene and related materials," 2D Mater. **7**, 022001 (2020).

[6] K. S. Novoselov, A. Mishchenko, A. Carvalho, and A. H. Castro Neto, "2D materials and van der Waals heterostructures," Science **353**, aac9439 (2016).

[7] A. K. Geim and I. V. Grigorieva, "Van der Waals heterostructures," Nature **499**, 419–425 (2013).

[8] M. H. Kalantari and X. Zhang, "Thermal transport in 2D materials," Nanomaterials **13**, 117 (2022).

[9] Y. Fu, J. Hansson, Y. Liu, S. Chen, A. Zehri, M. K. Samani, N. Wang, Y. Ni, Y. Zhang, Z. B. Zhang, Q. Wang, M. Li, H. Lu, M. Sledzinska, C. M. Torres, S. Volz, A. A. Balandin, X. Xu, and J. Liu, "Graphene related materials for thermal management," 2D Mater. **7**, 012001 (2020).

[10] D. L. Nika and A. A. Balandin, "Phonons and thermal transport in graphene and graphene-based materials," Rep. Prog. Phys. **80**, 036502 (2017).

[11] A. A. Balandin, "Thermal properties of graphene and nanostructured carbon materials," Nat. Mater. **10**, 569–581 (2011).

[12] D. A. Kez, A. M. Foley, F. W. B. H. Wong, A. Dolfi, and G. Srinivasan, "AI-driven cooling technologies for high-performance data centres: State-of-the-art review and future directions," Sustainable Energy Technol. Assess. **82**, 104511 (2025)..

[13] I. Latif, M. A. Shafique, H. Ullah, A. C. Newkirk, X. Yu, and A. Munir, "Cooling matters: Benchmarking large language models and vision-language models on liquid-cooled versus air-cooled h100 GPU systems," arXiv:2507.16781 (2025).

[14] H. Su, Y.-M. Lee, T. Peña, S. Fultz-Waters, J. Kang, C. Köroğlu, S. Wahid, C. J. Newcomb, Y. S. Song, H.-S. P. Wong, S. X. Wang, and E. Pop, "High-field breakdown and thermal characterization of indium tin oxide transistors," ACS Nano **19**, 16794–16802 (2025).

[15] C. Köroğlu and E. Pop, "High thermal conductivity insulators for thermal management in 3D integrated circuits," IEEE Electron Device Lett. **44**, 496–499 (2023).

[16] S. Shin, M. A. Wahab, M. Masuduzzaman, K. Maize, J. Gu, M. Si, A. Shakouri, P. D. Ye, and M. A. Alam, "Direct observation of self-heating in III–V gate-all-around nanowire mosfets," IEEE Trans. Electron Devices **62**, 3516–3523 (2015).

[17] G. Chen, "Non-fourier phonon heat conduction at the microscale and nanoscale," Nat. Rev. Phys. **3**, 555–569 (2021).

[18] D. G. Cahill, P. V. Braun, G. Chen, D. R. Clarke, S. Fan, K. E. Goodson, P. Keblinski, W. P. King, G. D. Mahan, A. Majumdar, H. J. Maris, S. R. Phillpot, E. Pop, and L. Shi, "Nanoscale thermal transport. II. 2003–2012," Appl. Phys. Rev. **1**, 011305 (2014).

[19] D. G. Cahill, W. K. Ford, K. E. Goodson, G. D. Mahan, A. Majumdar, H. J. Maris, R. Merlin, and S. R. Phillpot, "Nanoscale thermal transport," J. Appl. Phys. **93**, 793–818 (2003).

[20] M. P. Vallin, H. Yamaguchi, R. Karkee, C. Lee, R. M. Martinez, S. J. Fensin, J. B. Park, H. T. Vo, R. Z. Zhang, and M. T. Pettes, "Thermal conductivity of graphene coated copper under uniaxial tensile mechanical strain," Nanoscale Adv. **7**, 3655–3663 (2025).

[21] V. S. Saji, "2D hexagonal boron nitride (h-BN) nanosheets in protective coatings: A literature review," Heliyon **9**, e19362 (2023).

[22] D. Prasai, J. C. Tuberquia, R. R. Harl, G. K. Jennings, and K. I. Bolotin, "Graphene: Corrosion-inhibiting coating," ACS Nano **6**, 1102 (2012).

[23] D. Choi, N. Poudel, S. Park, D. Akinwande, S. B. Cronin, K. Watanabe, T. Taniguchi, Z. Yao, and L. Shi, "Large reduction of hot spot temperature in graphene electronic devices with heat-spreading hexagonal boron nitride," ACS Appl. Mater. Interfaces **10**, 11101 (2018).

[24] Z. Yan, G. Liu, J. M. Khan, and A. A. Balandin, "Graphene quilts for thermal management of high-power GaN transistors," Nat. Commun. **3**, 827 (2012).

[25]S. Subrina, D. Kotchetkov, and A. A. Balandin, "Heat removal in silicon-on-insulator integrated circuits with graphene lateral heat spreaders," IEEE Electron Device Lett. **30**, 1281 (2009).
[26]C. Monachon, L. Weber, and C. Dames, "Thermal boundary conductance: A materials science perspective," Annu. Rev. Mater. Res. **46**, 433–463 (2016).
[27]D. Estrada, Z. Li, G. M. Choi, S. N. Dunham, A. Serov, J. Lee, Y. Meng, F. Lian, N. C. Wang, A. Perez, R. T. Haasch, J. M. Zuo, W. P. King, J. A. Rogers, D. G. Cahill, and E. Pop, "Thermal transport in layer-by-layer assembled polycrystalline graphene films," npj 2D Mater. Appl. **3**, 10 (2019).
[28]W. Cai, A. L. Moore, Y. Zhu, X. Li, S. Chen, L. Shi, and R. S. Ruoff, "Thermal transport in suspended and supported monolayer graphene grown by chemical vapor deposition," Nano Lett. **10**, 1645–1651 (2010).
[29]Z. Chen, W. Jang, W. Bao, C. N. Lau, and C. Dames, "Thermal contact resistance between graphene and silicon dioxide," Appl. Phys. Lett. **95**, 161910 (2009).
[30]A. J. Schmidt, X. Chen, and G. Chen, "Pulse accumulation, radial heat conduction, and anisotropic thermal conductivity in pump-probe transient thermoreflectance," Rev. Sci. Instrum. **79**, 114902 (2008).
[31]H. Wang, Y. Xu, M. Shimono, Y. Tanaka, and M. Yamazaki, "Computation of interfacial thermal resistance by phonon diffuse mismatch model," Mater. Trans. **48**, 2349–2352 (2007).
[32]Y. Li, Y. Zhang, Y. Liu, H. Xie, and W. Yu, "A comprehensive review for micro/nanoscale thermal mapping technology based on scanning thermal microscopy," J. Therm. Sci. **31**, 976–1007 (2022).
[33]Y. Zhang, W. Zhu, F. Hui, M. Lanza, T. Borca-Tasciuc, and M. M. Rojo, "A review on principles and applications of scanning thermal microscopy (SThM)," Adv. Funct. Mater. **30**, 1900892 (2020).
[34]S. Gomes, A. Assy, and P.-O. Chapuis, "Scanning thermal microscopy: A review," Phys. Status Solidi A **212**, 477–494 (2015).
[35]A. Majumdar, "Scanning thermal microscopy," Annu. Rev. Mater. Sci. **29**, 505–585 (1999).
[36]M. Tortello, S. Colonna, M. Bernal, J. Gomez, M. Pavese, C. Novara, F. Giorgis, G. Saracco, R. S. Gonnelli, and A. Fina, "Effect of thermal annealing on the heat transfer properties of reduced graphite oxide flakes: A nanoscale characterization via scanning thermal microscopy," Carbon **109**, 390–401 (2016).
[37]Y. Li, J. Wu, J. Luo, J. Wang, W. Yu, and B. Cao, "Quantitative measurements in scanning thermal microscopy: Theoretical models, calibration technique, and integrated instrument," J. Appl. Phys. **138**, 050701 (2025).
[38]A. Charvátová Campbell, P. Klapetek, R. Šlesinger, J. Martinek, V. Hortvík, V. Witkovský, and G. Wimmer, "Calibration of scanning thermal microscopes using optimal estimation of function parameters by iterated linearization," Int. J. Therm. Sci. **218**, 110080 (2025).
[39]Z. Liu, Y. Feng, H. Li, N. Cao, and L. Qiu, "Quantitative analysis of interface heat transport at the $Si_3N_4/SiO_2$ van-der Waals point contact," Int. J. Heat Mass Transfer **232**, 125979 (2024).
[40]N. Fleurence, S. Demeyer, A. Allard, S. Douri, and B. Hay, "Quantitative measurement of thermal conductivity by SThM technique: Measurements, calibration protocols and uncertainty evaluation," Nanomaterials **13**, 2424 (2023).
[41]F. Menges, H. Riel, A. Stemmer, C. Dimitrakopoulos, and B. Gotsmann, "Thermal transport into graphene through nanoscopic contacts," Phys. Rev. Lett. **111**, 205901 (2013).
[42]M. Tortello, I. Pasternak, K. Zeranska-Chudek, W. Strupinski, R. S. Gonnelli, and A. Fina, "Chemical-vapor-deposited graphene as a thermally conducting coating," ACS Appl. Nano Mater. **2**, 2621–2633 (2019).
[43]P. S. Dobson, J. M. Weaver, and G. Mills, "New methods for calibrated scanning thermal microscopy (SThM)," in *Sensors* (IEEE, 2007), pp. 708–711.
[44]A. Assy, "Development of two techniques for thermal characterization of materials: Scanning thermal microscopy (SThM) and $2\omega$ method," Doctoral thesis (INSA de Lyon, 2015).
[45]C. J. Shearer, A. D. Slattery, A. J. Stapleton, J. G. Shapter, and C. T. Gibson, "Accurate thickness measurement of graphene," Nanotechnology **27**, 125704 (2016).
[46]J. H. Seol, I. Jo, A. L. Moore, L. Lindsay, Z. H. Aitken, M. T. Pettes, X. Li, Z. Yao, R. Huang, D. Broido, N. Mingo, R. S. Ruoff, and L. Shi, "Two-dimensional phonon transport in supported graphene," Science **328**, 213–216 (2010).

# Supplemental material of
# Analysis of Scanning Thermal Microscopy Measurements on CVD Graphene

Han Zhang,[1] Andrea Napolitano,[1] and Mauro Tortello[1]

*Dipartimento Scienza Applicata e Tecnologia, Politecnico di Torino,*
*Cso Duca degli Abruzzi 24, 10129 Torino (TO), Italy*

(*Electronic mail: mauro.tortello@polito.it)

(Dated: 19 March 2026)

## I. FINITE-ELEMENT MODEL OF THE STHM PROBE

A fully three-dimensional coupled thermal-electric model was developed by using the commercial software COMSOL Multiphysics 6.3, which combines heat transfer and electric current equations within the finite-elements method framework. In order to have a more accurate result, the thin layer feature has been implemented. A steady-state thermal analysis was performed to investigate the heat transfer behavior during SThM measurements since the adopted scanning rate, 0.5 Hz, is sufficient to reach the steady state at each measurement pixel[1]. The heat conduction can be described by:

$$-\nabla \cdot (k \nabla T) = Q \tag{S1}$$

where $k$ is the thermal conductivity, $T$ the temperature and $Q$ the heat source, i.e., the heat transferred by the Pd film by means of the Joule effect. In equation S1, the boundary conditions can be either a specified temperature or heat flux. In our simulations, the specified heat boundary conditions are of constraint type and prescribe a fixed temperature on a boundary i.e., $T = T_0$ on $\partial\Sigma$, where $\Sigma$ represents the whole computational domain consisting of air, probe, and graphene with the substrate. $\partial\Sigma$ represents a domain boundary. The probe consists of three components: $Si_3N_4$ as the main material for the probe and cantilever, Au electrodes and the Pd film. Au electrodes are used to deliver current to and from the Pd film deposited at the probe apex. The SThM probe used in the experiments analyzed in this paper was carefully modeled in terms of materials and geometry: Au thickness is 140 nm and the substrate for the probe is a 0.65 $\mu$m thick $Si_3N_4$ plate. One end of the plate has a triangular shape with a tip angled away of 55° from the substrate plane, while the nominal Pd thickness is 40 nm. However, as discussed later, the latter parameter was slightly changed in order to validate the model in the isotropic case. The structure of the probe is shown in Fig. 2(a) of the main text and in Fig. S1(a).

The initial temperature was set to $T_{ref} = 24$ °C for all domains, corresponding to the room temperature. The outer air region was modeled as an infinite element domain, and this temperature was fixed to $T_{ref}$. Likewise, the outer boundaries of the substrate were set to the specified $T_{ref}$, as well. This was necessary to reach the equilibrium in the stationary simulation which would otherwise diverge, because of the heat source. Indeed, heat is generated at the Pd film and flows into the surrounding air and into the cantilever and sample. A current equal to $I_0 = 1.35$ mA, the same used in the experiments[2], is sourced to one terminal of the electrical circuit. The electric potential and current distribution are then computed in all the conductive layers, while the other end of the circuit is grounded and serves as a reference, providing the return path. All other domain boundaries are electrically insulated, to ensure that the current closes only through the intended conductive path. The probe-sample contact area can be tuned by changing the size of the cross section of the probe in contact with the sample. The contact area, $A$ can be related to the contact radius, $r$ through the relationship $A = \pi r^2$. Indeed, depending on the substrate, the contact radii were set to $r = 20 \div 60$ nm for $SiO_2$ and $Al_2O_3$, and $r = 60 \div 90$ nm for PET, as it was found in ref.[2]. Across interfaces between different domains, temperature and heat flux density are assumed to be continuous, the thermal boundary resistance (TBR) between tip and sample is $r_{ts} = (2.4 \pm 0.6) \times 10^{-8}\ \mathrm{K \cdot m^2/W}$ [2]. $r_{ts}$ is modeled as 25 nm thick element added between the tip and the sample, as schematically shown in Fig. 2(b) and (c) of the main text.

The thermal-electric coupled model was discretized primarily with free tetrahedral elements, which provide robust meshing capability for complex 3D geometries. The substrate domain was placed in a rectangular computational chamber, and the surrounding air was modeled using an infinite element domain to simulate an open space. The chamber mesh was generated using the swept meshing operation. In this meshing strategy, the surface mesh generated on a source face is propagated through the domain toward the opposite destination face, yielding a semistructured mesh that is well suited for high-aspect-ratio regions, helps to control elements distortion, and improves numerical stability. The temperature and electric potential distributions were approximated using quadratic (second-order) Lagrange shape functions, which enhance the accuracy in resolving field gradients compared with linear interpolation.

The reliability of the numerical results and computation time are dependent on the mesh quality. Therefore, a multi-resolution mesh was employed. In particular, for the regions that dominate the thermal response, Pd tip and tip-sample contact area, a strongly graded mesh was adopted, with the finest discretization concentrated at the Pd apex. This level of refinement was chosen to guarantee numerical accuracy in the sensing region by sufficiently resolving the temperature gradients near the tip–sample interface. The reproducibility of the results was checked at increasing number of mesh elements, i.e., reduced elements size, in order to ensure that the outcome is reliable while at the same time keeping a reasonable computation time.

Fig. S1(b) shows the thermal probe in air, at a distance of approximately 1 $\mu$m from the substrate, PET in this case. The average temperature of the probe is $T_p = 70.3\ ^\circ\mathrm{C}$. The temperature is averaged over the whole Pd film, which is the most reasonable choice for the comparison with the experiments in which the temperature is determined by the overall variation of the Pd film

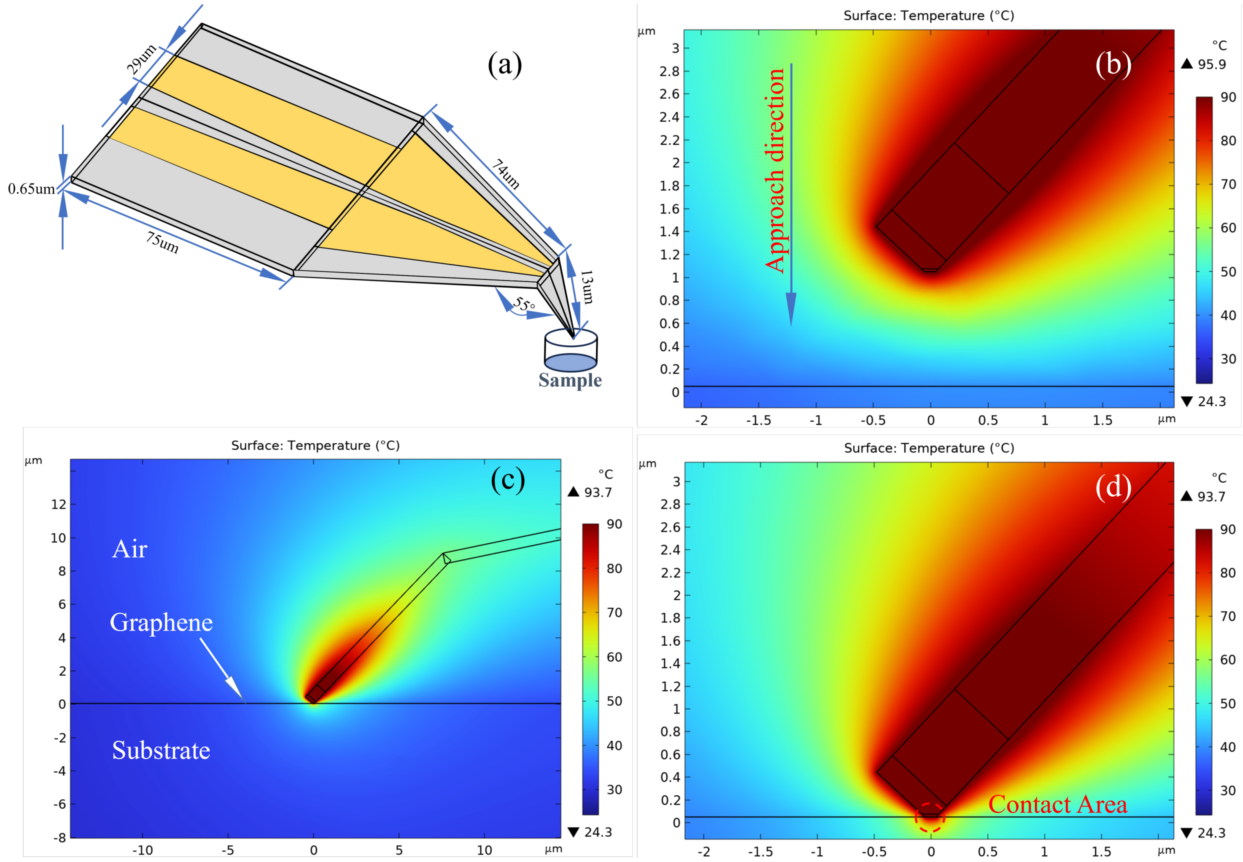

FIG. S1. (a) Geometrical model of the SThM Pd probe adopted for the FEA simulations, along with the characteristic dimensions. (b) Temperature map of the probe, heated by means of the Joule effect caused by a current $I_0 = 1.35$ mA, suspended far from the sample. (c) Same as in (b) but with the probe in contact with a PET substrate. (d) Magnified view of panel (c), with indication of the tip-sample contact area.

resistance in the Wheatstone bridge. It is possible to see that the probe is heating the surrounding air, whose temperature decreases moving away from the tip. When the probe comes into contact with graphene, the temperature decreases to $T_p = 69$ °C, due to the additional heat transfer into the sample both through air and solid-solid channel, as shown in Fig. S1(c) and (d).

## II. POSSIBLE NON-DIFFUSIVE HEAT TRANSFER MECHANISMS

Since the Pd probes adopted in this work operate at the nanoscale, we may observe several phenomena that deviate from the diffusive heat transfer mechanism. A large amount of the probe-sample heat exchange occurs through air conduction. Very close to the probe apex, the mean free path of air molecules is larger than the distance from the sample and therefore quasi-ballistic conduction may occur. The mean free path is about 60-70 nm[3] and FEM is not taking this effect into account. However, we can notice that the region in which ballistic conduction of air is taking place is very small compared to the overall volume in which probe-sample heat transfer is occurring through the air. Indeed, the surface area of Pd (the heating element) that is distant less than 100 nm from the sample is $S_{100} \cong 0.02\ \mu\text{m}^2$, very small compared to the whole Pd surface area, $S \cong 15\ \mu\text{m}^2$. Therefore, we assume that ballistic air conduction should have a small influence in these experiments.

Furthermore, also the solid-solid heat conduction channel through the tip sample contact could feature a non-Fourier heat transfer mechanism. The contact radii used in the simulations, and estimated from the experiments, are all in the range of the tens of nanometers. This situation implies a diffusive regime for PET and $SiO_2$ for which the phonon mean free path is only a few nm[4]. As for the $Al_2O_3$, in the lower range of simulated contact radii the quasi-ballistic regime might be involved[5]. In that case, the spreading resistance of the substrate could be for example modified with a corrected thermal conductivity that accounts for the thermal conductivity suppression due to the quasiballistic regime[6,7]. However, given the wide experimental uncertainty range, we did not consider necessary to introduce this effect here, because it would only partially affect the results. As for graphene, its mean free path is strongly reduced when it is supported due to the interaction with the substrate, being around 100 nm[8]. Moreover, the presence of grains, impurities, adsorbates, and wrinkles will further reduce it, decreasing, for example, to 20 nm in case of nanoribbons[9]. As it is possible to see in ref[2], our samples showed a quite irregular surface, with defects on a length scale of a few tens of nanometers which certainly further reduced the mean free path. Therefore, also in this case we did not consider quasi ballistic conduction of graphene in the FEM analysis.

## III. TEMPERATURE-INDUCED DEFORMATIONS

The effect of temperature-induced deformations was investigated as well. For this, we coupled the solid mechanics module with the heat transfer one to account for deformations in both the probe and the sample. The temperature distribution in the probe and sample was first computed using the heat transfer module. These results were then used as input for the solid mechanics module, which calculates the thermal displacement caused by the temperature gradients. As a boundary condition, the bottom surface of the sample is fixed. We first considered the PET substrate which exhibits the

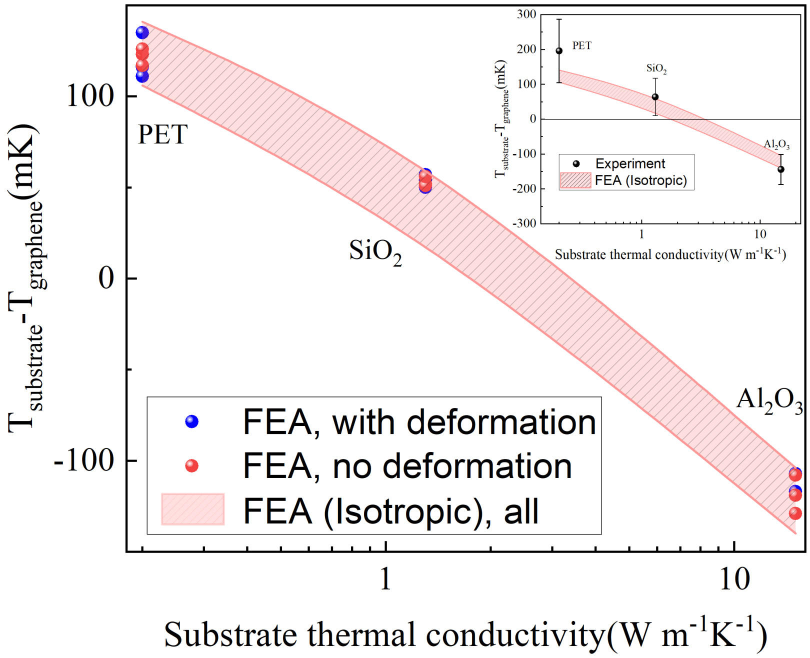

FIG. S2. Blue and red symbols are the simulated temperature differences $\Delta T = T_{substrate} - T_{graphene}$ for graphene supported by different substrates, considering temperature-induced deformations or neglecting them, respectively. Red band: FEA simulation results with $k_{eff} = 2.5 \pm 0.3$ W/(m·K) and $t_{eff} = 3.5 \pm 0.3$ nm. Inset: FEA results (red band) along with the experimental results, as reported also in Fig. 3(c) of the main paper.

largest deformation in the model because it has the highest thermal expansion coefficient among the materials considered. The average temperature of the probe in the model including deformations was 68.95 °C, compared to 68.94 °C, obtained from the model without deformation. Thus, the effect on the temperature in the worst case of PET could be deemed scarcely relevant. This conclusion is strengthened by considering that, in our analysis, we always considered temperature differences, $T_{substrate} - T_{graphene}$ which means that the effects of deformations tend to cancel out, since we always considered small temperature differences. However, to investigate the impact of the temperature-induced deformations more precisely, we calculated, for each substrate, three cases including deformations and compared them with their relevant counterpart in which this effect is neglected. The results are shown along with the band representing the whole range of FEA results, in Fig. S2. No appreciable difference can be observed between simulation results including deformations (blue symbols) and those without (red symbols), apart from the case of PET, for which a small discrepancy is visible, indicating however that temperature-induced deformations do not have a relevant effect on the temperature distribution.

## IV. NATURAL CONVECTION

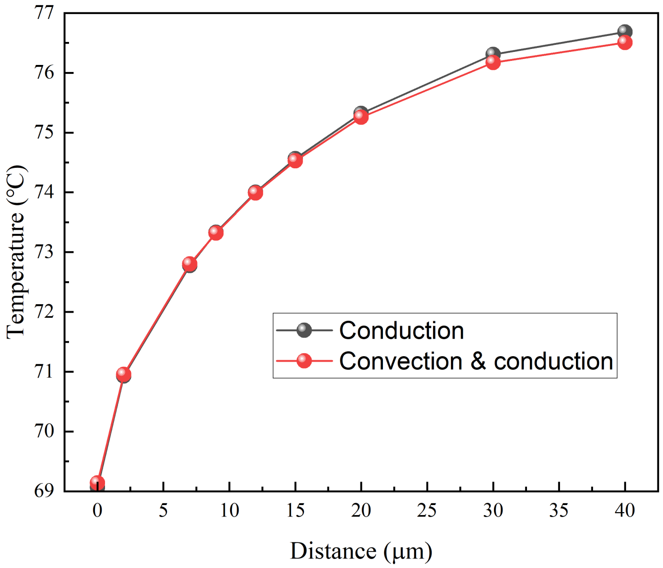

FIG. S3. Simulated probe temperature as a function of the tip-sample distance. Black symbols account only for the effect of air conduction while red symbols have been obtained by considering also the effect of natural convection on the heat flux at the probe surface.

Finally, we performed further simulations accounting for the modification to the heat flux at the probe surface due to natural convection, similarly to what was done by Lefèvre et al.,[10] in the case of the Wollaston wire probe. The following boundary condition was imposed on the heat flux at the probe surface:

$$q_0 = h(T_{ext} - T)$$

with $q_0 = -\mathbf{n} \cdot \mathbf{q}$. Here, $\mathbf{q}$ is the flux vector, $\mathbf{n}$ the normal vector of the boundary, and $q_0$ the inward heat flux. $T$ is the local boundary temperature, $T_{ext}$ the temperature far from the domain, and $h$ the effective heat transfer coefficient which also accounts for natural convection. The heat transfer coefficient was set to $h = 25\ \mathrm{W}/(\mathrm{m}^2 \cdot \mathrm{K})$ to effectively represent the overall cooling capacity of the air[11] while $T_{ext} = T_{ref} = 24^\circ$ C. Fig. S3 shows the probe temperature at increasing distance from the sample. Two cases are reported: one in which natural convection is not considered and the other with convection. It is possible to notice that the temperature, close to the sample, coincides in the two cases. As expected, the temperature of the probe is lower when convection is taken into account, due to its additional cooling effect. However, the deviation from the case in which this effect is neglected is observed only at large distances, i.e., in a configuration different than the one studied in this work. Indeed, in our case the probe is always in contact with the sample. Moreover, when accounting for the effect of natural convection in the simulations, the computational time is considerably longer. Therefore, we have not included it in our model.

## REFERENCES

[1] E. N. Esfahani, F. Ma, S. Wang, Y. Ou, J. Yang, and J. Li, "Quantitative nanoscale mapping of three-phase thermal conductivities in filled skutterudites via scanning thermal microscopy," National Science Review **5**, 59–69 (2018).

[2] M. Tortello, I. Pasternak, K. Zeranska-Chudek, W. Strupinski, R. S. Gonnelli, and A. Fina, "Chemical-vapor-deposited graphene as a thermally conducting coating," ACS Applied Nano Materials **2**, 2621–2633 (2019).

[3] S. G. Jennings, "The mean free path in air," Journal of Aerosol Science **19**, 159–166 (1988).

[4] M. Li, L. Dai, H. Wu, Y. Yan, J. S. Kang, S. King, P. E. McNeil, D. Butts, T. Galy, M. Marszewski, E. Lan, B. S. Dunn, S. H. Tolbert, L. Pilon, and Y. Hu, "Ballistic transport from propagating vibrational modes in amorphous silicon dioxide: Thermal experiments and atomistic-machine learning modeling," Materials Today Physics **51**, 101659 (2025).

[5] J. Tiwari and T. Feng, "Accurate prediction of thermal conductivity of $Al_2O_3$ at ultrahigh temperatures," Physical Review B **109**, 075201 (2024).

[6] B. Vermeersch and N. Mingo, "Quasiballistic heat removal from small sources studied from first principles," Physical Review B **97**, 045205 (2018).

[7] H. L. Li, J. Shiomi, and B. Y. Cao, "Ballistic-diffusive heat conduction in thin films by phonon monte carlo method: Gray medium approximation versus phonon dispersion," Journal of Heat Transfer **142**, 112502 (2020).

[8] E. Pop, V. Varshney, and A. K. Roy, "Thermal properties of graphene: Fundamentals and applications," MRS Bulletin **37**, 1273–1281 (2012).

[9] A. Y. Serov, Z. Y. Ong, and E. Pop, “Effect of grain boundaries on thermal transport in graphene,” Applied Physics Letters **102**, 033104 (2013).

[10] S. Lefèvre, S. Volz, and P. O. Chapuis, “Nanoscale heat transfer at contact between a hot tip and a substrate,” International Journal of Heat and Mass Transfer **49**, 251–258 (2006).

[11] F. P. Incropera, D. P. DeWitt, T. L. Bergman, and A. S. Lavine, *Fundamentals of Heat and Mass Transfer*, 6th ed. (John Wiley & Sons, New York, 1996).